NOVEMBER 1981

PPPL-1843
UC-20B

PPPL--1843

DE82 005724

A MONTE CARLO MODEL OF NEUTRAL-PARTICLE TRANSPORT IN DIVERTED PLASMAS

BY

D. HEIFETZ, D. POST,
M. PETRAVIC, J. WEISHEIT,
AND G. BATEMAN

PLASMA PHYSICS LABORATORY

PRINCETON UNIVERSITY
PRINCETON, NEW JERSEY

This work was supported by the U.S. Department of Energy Contract No. DE-AC02-76-CHO 3073. Reproduction, translation, publication, use and disposal, in whole or in part, by or for the United States government is permitted.

A MONTE CARLO MODEL OF NEUTRAL PARTICLE TRANSPORT IN DIVERTED PLASMAS

D. Heifetz, D. Post, M. Petravic, J. Weisheit, and G. Bateman*

Plasma Physics Laboratory, Princeton University

Princeton, New Jersey 08544

ABSTRACT

The transport of neutral atoms and molecules in the edge and divertor regions of fusion experiments has been calculated using Monte-Carlo techniques. The deuterium, tritium, and helium atoms are produced by recombination in the plasma and at the walls. The relevant collision processes of charge exchange, ionization, and dissociation between the neutrals and the flowing plasma electrons and ions are included, along with wall reflection models. General two-dimensional wall and plasma geometries are treated in a flexible manner so that varied configurations can be easily studied. The algorithm uses a pseudo-collision method. Splitting with Russian roulette, suppression of absorption, and efficient scoring techniques are used to reduce the variance. The resulting code is sufficiently fast and compact to be incorporated into iterative treatments of plasma dynamics requiring numerous neutral profiles. The calculation yields the neutral gas densities, pressures, fluxes, ionization rates, momentum transfer rates, energy transfer rates, and wall sputtering rates. Applications have included modeling of proposed INTOR/FED poloidal divertor designs and other experimental devices.

---

*Permanent address: Georgia Institute of Technology, Atlanta, GA.

TABLE OF CONTENTS

ABSTRACT

I. INTRODUCTION

II. THE PHYSICAL MODEL

A. Geometric and Plasma Parameters

B. Neutral-Plasma Reactions and Hydrogen versus Helium Transport

C. Wall Reflection Models

III. THE MONTE-CARLO ALGORITHM

A. Flight Initialization

B. Flight Tracking

C. Test Flux Weighting

D. Integration Methods

E. Variance Reduction Techniques

F. Code Optimization and Performance

IV. ILLUSTRATIVE CALCULATIONS

A. The Vacuum Case

B. The PDX Scoop Experiment

C. The Proposed INTOR Design

I. INTRODUCTION

A key problem in the design of reactor-sized fusion experiments is the control of particle and heat exhaust. The helium ash produced by the fusion reaction $D + T \rightarrow He_3 + n$ must be removed for long pulse reactor operation. However, the helium removal technique must minimize the pumping of tritium. Thermal heat exhaust must be achieved without introducing impurities into the main plasma. Poloidal divertors and pump limiters have been proposed to solve these problems [1].

The performance of divertors and pump limiters depends crucially on the transport of the neutrals created in the device. For example, a design study [1] for the INTOR tokamak uses a single null poloidal divertor, shaping the magnetic field so that the plasma at the edge flows into a divertor chamber (Fig. 1a). In the divertor chamber (Fig. 1b), the plasma flows along the field lines until it reaches the neutralizer plate, where an electrostatic sheath forms to keep the ion and electron currents equal. The ions are accelerated across the sheath and recombine to form neutrals at the plate. The neutrals then travel down the divertor and the pump, transporting mass, momentum, and energy as they collide with the plasma and walls.

In this paper, we describe an algorithm developed to model this transport using Monte-Carlo techniques, which is flexible enough to be applied to a wide range of divertor problems. For a given particle, energy flux profile, and geometry, we compute (1) the conductances for hydrogen and helium down pumping channels or against the instreaming plasma, and the relative pumping efficiencies for hydrogen and helium, (2) the power loads and erosion rates at the chamber walls, and (3) the ionization and charge-exchange particle, momentum and energy exchange rates in the plasma, and the neutral densities and pressures in the exhaust channel. We also note that the techniques

developed here are directly applicable to a wide range of questions outside of tokamak modeling.

Section II of this paper presents the physical models used in the treatment of plasma profile and wall configurations, neutral-plasma reactions, and neutral-wall interactions. In Section III we discuss the Monte-Carlo algorithm. The overall approach is a standard one, and we note only these aspects unique to our problem. In particular, the pseudo-collisional method of tracking test fluxes is described. Test fluxes deposit scorings of ionizations and charge exchanges at each pseudo-collision from which neutral temperatures and densities are derived. A sub-algorithm efficiently models wall reflections using Monte-Carlo data from the MARLOWE code [2]. Suppression of test particle absorption and partial vectorization of the computer code economize code operation. Finally, Section IV gives three example calculations: for a vacuum, for an experiment conducted on the PDX experimental device, and for an INTOR design.

Callen et al. [3] review our modeling results for advanced divertor design, as well as presenting a detailed comparison with the calculations of Seki et al. [4]. The code has been incorporated also into a self-consistent fluid model of divertor plasmas [5].

II. THE PHYSICAL MODEL

A basic assumption is that plasma conditions are constant throughout the flights of the Monte-Carlo test flights. For experiments in equilibrium for > 100 msecs, a time independent approach is then valid. However, when the timescale of change is a few tens of microseconds, a time dependent approach is necessary. We only describe here the time independent model. This model could be modified easily into a time dependent one.

A. Geometric and Plasma Parameters

Plasma zone boundaries and chamber walls vary two-dimensionally in the x-y plane, and are assumed to be infinite in the z-direction. They are described by piecewise linear approximations. A representative sample of configurations which have been used is shown in Fig. 2.

The plasma density, temperature, and flow velocity is specified for each zone individually before the calculation. The plasma flux on the walls, with the appropriate particle reflection and sheath models, provides the source flux boundary conditions for the neutral transport calculation.

B. Neutral-Plasma Reaction and Hydrogen versus Helium Transport

The collision processes considered most important to our calculations and included in it are listed in Table I. Reactions such as

$$e^- + H_2^o \rightarrow H^+ + H^+ + 3e^- ,$$

$$e^- + H_2^+ \rightarrow H^+ + H^+ + 2e^- ,$$

have appreciably smaller cross sections than competing reactions, and so are not included.

The cross sections for the reactions in Table I are computed from numerical fits in Freeman and Jones [6] and Jonas [7], and are used to compute tables of $\langle\sigma v\rangle$ as a function of neutral energy E_o and plasma ion temperature T_i, using Gauss-Hermite quadrature.

A measure of the relative importance of each reaction can be obtained from the reaction rates $n\langle\sigma v\rangle$ where n is a typical density chosen for the plasma ions (D^+, T^+, or He^{++}) or electrons (Figs. 3A, 3C). The dominant reaction for neutral hydrogen at all energies is charge exchange (Fig. 3B). Ionization for neutral hydrogen is almost comparable to charge exchange at

T ~ 40-60 eV, but it is much less at lower temperatures. This contrasts with the situation for neutral helium where ionization dominates helium-helium charge exchange for T > 4 eV. Helium-hydrogen charge exchange is important only at high temperatures (> 2 keV).

The relative neutral/ion yield rates from H_2^o dissociations by electrons are plotted in Fig. 4 as a function of electron temperature T_e. For T_e < 10 eV, the dominant reaction is $e + H_2^o \rightarrow 2H^o + e$, so that almost all dissociating hydrogen is atomic. Above ~ 10 eV, electron ionization followed by dissociation into $H^o + H^+ + e$, becomes important, and for T_e > 100 eV, half the hydrogen produced by dissociation is atomic. Also, since the velocity of the molecules is low (~ 10^5cm/sec) having been desorbed off a wall (see Sec. II.C), the mean free path of the molecules is shorter than energetic hydrogen neutrals (~ 3 eV, v ~ 10^6cm/sec). This results in about one-half of the hydrogen atoms that leave the wall as molecules being ionized very close to the wall.

The ordering of reaction rates for hydrogen and helium is important for the relative transport of neutral hydrogen versus neutral helium in a plasma. It has been argued [4] that the plasma acts as a helium filter. Since hydrogen neutrals can charge exchange with the hot ions in the plasma, some of the energy lost by collisions with the wall can be recovered by the neutral hydrogen atoms, and thus keep the mean free path for ionization large. Helium atoms, however, would be "re-energized" by charge exchange to a much less degree than hydrogen. This is because the charge exchange cross sections for helium with helium are smaller, and the percentage of helium ions in the plasma is small (~ 5% of n_e) compared with hydrogen (~ 90% of n_e). Thus, the helium atoms would be expected to slow down by wall collisions and might be ionized more rapidly than the hydrogen atoms.

The situation is complicated, however, by the fact that the hydrogen mean free path for charge exchange is about one-half of the mean free path for ionization. Thus there will be about two charge-exchange collisions for each ionizing collision. If we assume a simplified model with neutral hydrogen atoms resulting from charge-exchange collisions isotropically distributed, the directed motion of neutrals down the divertor duct will be lost. Charge exchange for hydrogen thus helps the transport of hydrogen neutrals down the divertor by restoring the energy lost by wall collisions, but it also hurts the transport by randomizing the velocities of the neutral atoms. Further complicating the picture is the lower ionization rate of helium compared to hydrogen and the production of cold hydrogen molecules at the wall as described in Section II.C. We have found in the INTOR case described in Section III that the net result of all these competing effects is that hydrogen and helium neutrals have similar transport rates at moderate plasma densities ($\sim 10^{12} - 10^{13} cm^{-3}$).

C. Wall Reflection Models

Two models for reflecting neutral atoms and ions from the divertor walls are included. The first is similar to that of Seki [4] for iron. If θ is the incident polar angle (Fig. 5), and E the incident energy in eV, the reflection coefficient is

$$R_N = \begin{cases} -0.237 \ln(E/\alpha) + 0.19 , & \theta \leq 40^\circ \\ 1 , & \theta > 40^\circ \end{cases} ,$$

with α = 2990., 2990., and 6290. for D°, T°, and He° respectively. The reflected velocity cosines $(V_x(out), V_y(out), V_z(out))$ vary from specular for $\theta \sim 90^\circ$, to a cosine distribution in polar angle for $\theta \sim 0^\circ$. We used the formulas

$$V_x(\text{out}) = [\cos\theta \sin\alpha + \sin\theta \cos\phi \cos\alpha] \cos\zeta - \sin\theta \cdot \sin\phi \cdot \sin\zeta,$$

$$V_y(\text{out}) = [\cos\theta \cdot \sin\alpha + \sin\theta \cos\phi \cos\alpha] \sin\zeta + \sin\theta \cdot \sin\phi \cdot \cos\zeta,$$

$$V_z(\text{out}) = \cos\theta \cos\alpha - \sin\theta \cos\phi \sin\alpha,$$

where

$$\cos\alpha = -V_z(\text{in}) ,$$

$$\cos\zeta = V_x(\text{in})/\left(V_x(\text{in})^2 + V_y(\text{in})^2\right)^{1/2} ,$$

$$\sin\theta = \cos\alpha \sqrt{\xi} ,$$

and

$$\phi = 2\pi\eta ,$$

ξ, η being uniform random numbers between 0 and 1. The energy of the reflected neutral is taken to be

$$E(\text{out}) = \begin{cases} \left(-0.22 \ln [E(\text{in})/\alpha] + 0.06\right)/R_N , & \theta \leq 40^\circ \\ 0.9E(\text{in}) , & \theta > 40^\circ \end{cases} .$$

Hydrogen and helium not reflected is assumed to desorb eventually (in steady state) as molecules or atoms, mono-energetically at the wall temperature, and with a cosine distribution in polar angle. Molecules striking the wall do so at low velocity and are assumed to desorb immediately,

with the same cosine distribution assumed for desorbed H and He atoms.

For our second model we use data from the Monte-Carlo code MARLOWE which computes trajectories of test particles striking a wall and scattering off the atoms in the crystalline lattice of the wall, ultimately coming to rest in the wall or escaping with a reduced velocity. For each species of incident test flux, assuming in our case a smooth amorphous wall of iron, a scattering distribution is computed which is a five-dimensional differential distribution $P(v,\theta,\phi,E,\alpha)\ v^2\ dv\ \sin\theta\ d\theta\ d\phi$, in terms of incident energy E, incident polar angle α, and outgoing speed V, polar angle θ, and azimuthal angle ϕ relative to the plane of the incident test flux and wall normal (Fig. 5). The fraction of incident particles reflected as a function of incident E and α is also computed.

Given incident E and α, the three-dimensional distribution

$$P_{E,\alpha}(v,\theta,\phi)\ v^2\ dv\ \sin\theta\ d\theta\ d\phi,$$

must be sampled. Now $P\ v^2 dv\ \sin\theta\ d\theta\ d\phi$ will be highly peaked at points, both for physical reasons and because of too few Monte-Carlo scorings for a smooth result. Thus care must be taken in designing a fast sampling algorithm which is economical in storage.

In our algorithm we first reduce the sampling of $P\ v^2 dv\ \sin\theta\ d\theta\ d\phi$ to sampling consecutively from the three one-dimensional distributions f^1, f^2, and f^3, defined by

$$f^1_{E,\alpha}(v) = \iint P_{E,\alpha}(v,\theta,\phi)\ \sin\theta\ d\theta\ d\phi\ ,$$

$$f^2_{E,\alpha}(\theta) = \int P_{E,\alpha}(v_o,\theta,\phi)\ d\phi\ ,$$

and

$$f^3_{E,\alpha}(\phi) = P_{E,\alpha}(v_o, \theta_o, \phi) \ .$$

These distributions are stored as follows. Each distribution is given by n data points $x_1 \leq x_2 \leq \ldots \leq x_n$. For $0 < \xi < 1$, if $(i/n) \leq \xi < [(i+1)/n]$ set $x_\xi = x_i$. Then we store x_ξ, for $\xi = 0.1$, 0.3, 0.5, 0.7, and 0.9, for each distribution of f^1, f^2, and f^3 forming the arrays $F^1_{E,\alpha}(\xi)$, $F^2_{E,\alpha}(\eta,\xi)$, and $F^3_{E,\alpha}(\zeta,\eta,\xi)$, using $\alpha = 0^o$, 20^o, 40^o, 60^o, 80^o, and $E = 50$, 100, 200, 500, and 1,000 eV. Thus, the largest array needed, $F^3_{E,\alpha}$, has size $5^5 = 3124$.

For example, Table II gives F^1, F^2, and F^3, for $E = 200$ eV, $\alpha = 0^o$. The reflection coefficient is 0.4320. If a reflection occurs, three choices of a uniform random variable on the unit interval are made, say $\xi = 0.3$, $\eta = 0.5$, and $\zeta = 0.9$. Then $v = F^1(2) = 100$ eV, $\cos\theta = F^2(3,2) = 0.6497$, and $\cos\phi = F^3(5,3,2) = -0.5448$ (it is more convenient to store $\cos\theta$ and $\cos\phi$ than θ and ϕ). For more general ξ, η, and ζ, we derive v, $\cos\theta$, and $\cos\phi$ through linear interpolation of F^1, F^2, and F^3.

Wall sputtering rates for various materials were fit from the data of Roth et al. [8]. The angular dependence of the rate was assumed to be proportional to [cos (polar angle)]$^{(-1.5)}$.

III. THE MONTE-CARLO ALGORITHM

In our time independent calculation a profile consists of a set of test flux flights (Fig. 6). This section describes how these flights are initiated, flown, and integrated to yield the physical parameters of interest.

A. Flight Initialization

Two neutral sources are modeled, a volume source due to recombination and

a wall source. For greater computational clarity independent profiles are made for each source.

In the recombination profile each test particle represents ω_b = γ(recomb)/N real particles per second, where γ(recomb) = total recombination rate of the plasma [9] and N is a suitable number of test flights (typically 500 < N < 2,000). The initial position is selected from the 2-D distributions of recombination rates over the plasma region, and the initial velocity sampled from a 3-D Maxwellian at the local ion temperature is shifted by the local flow velocity.

The wall source of neutrals comes from ions either flowing into the neutralizer plate or diffusing to a side wall. Given a 1-D ion flux distribution hitting the wall from a separate computation, initial positions at the wall are selected with each test particle now representing ω_b = γ(wall)/N real particles per second, where γ(wall) is the total flux on the walls, and N again is the total number of test flights. Initial energy is determined by assuming that the initial ion energy is increased at the wall by a selected sheath potential and then attenuated by striking normal to the wall and reflecting or sticking.

B. Flight Tracking

Given the initial position P_o, velocity v and atomic species, we are ready to begin the test flight. We have a choice between two tracking algorithms, the path length estimator method and the pseudo-collision algorithm. The path length estimator method is based on path length estimators similar to that in [11] and is described in Fig. 7. The pseudo-collision algorithm is based on the idea of pseudo-collisions suggested to us by S. V. Putvinsky [10]. Our version is flow charted in Fig. 8.

At the beginning of each profile, two 2-dimensional arrays $R_1(i,j)$ and $R_2(i,j)$ containing plasma zone indices in a finer uniform rectangular grid are constructed (Fig. 9). Given a position P in the device, its coordinates $(i_p j_p)$ in the reference meshes are easily computed, and its plasma zone coordinates $I = R_1(i_p,j_p)$, $J = R_2(i_p,j_p)$ looked up, determining the plasma conditions at P.

The pseudo-collisional algorithm uses this information as follows. Choosing the number of mean free paths $\mu = -\log\xi$, ξ a uniform random variable, $0 < \xi \leq 1$, the test flux is moved a distance $\mu \cdot \lambda(\min)$, where $\lambda(\min)$ the shortest mean free path length in the entire given plasma for a test flux with the velocity V. Assuming a wall has not been hit, the local mean free path length at the new position, $\lambda(\text{local})$, is computed using the reference arrays. The ratio $\rho = \lambda(\min)/\lambda(\text{local})$ represents the probability that a real collision occurs at the new point. If a test does not result in a collision, we say a pseudo-collision has occurred, and we repeat the process choosing a new μ, moving a distance $\mu \cdot \lambda(\min)$ and so on until the test flux hits a wall, leaves the device, or finally does undergo a plasma collision.

These two algorithms have somewhat complementary disadvantages in tracking. A disadvantage of the path length estimator method is the time consuming geometric calculations required in computing the points P_i and distances d_i (Fig. 7). An advantage of the pseudo-collisional algorithm over the path length estimator algorithm is that the reference arrays contain the only detailed geometric calculation necessary, and the algorithm described above to compute them is quite efficient, computing 300 x 300 reference arrays in less than 1 cpu second on the CRAY-1 and packing the arrays so as to reduce storage. The amount of geometric calculation is independent of the number of test fluxes flown.

A disadvantage of the pseudo-collision algorithm is that λ(min) must be computed. A table of λ(min) must be made at the start of a set of profiles as a function of neutral velocity, species, plasma density, and temperature. However, the algorithm requires only that the step size be no longer than λ(min), so smaller lengths derived from worst case study of $n\langle\sigma v\rangle$ rates remove the need for the large λ(min) table. Underestimating λ(min) though means more test steps to a collision, reducing efficiency, so care must be used in choosing λ(min).

C. Test Flux Weighting

Both the path length estimator method and the pseudo-collision algorithm use the method of suppressed absorption. At each collision, the charge exchanging probability,

$$P_{cx} = \lambda(c\text{-}x)/\lambda(\text{local}) ,$$

is computed, where λ(c-x) is the local mean free path length due to charge exchange only. The test flux is then "split" between ionization and charge exchange by reducing its weight ω to $P_{c-x}\omega$. Thus, a test flux weight of $\omega_i = (1 - P_{c-x})\ \omega$ is ionized.

If, however, ω falls below a given minimum, this "splitting" is stopped, and a choice is made among a pure charge exchange, continuing the flight with ω unchanged, or pure ionization, setting ω = 0, and ending the flight.

After modifying ω in the suppressed absorption algorithm, ω is scaled by a factor $\kappa = \sigma|v|/\langle\sigma v\rangle$ to account for the charge-exchange cross sections being nonconstant over the Maxwellian distribution of ions. Thus energy is conserved. We do not at present include any angular dependence in our charge exchange model.

D. Integration Methods

Integrating flights in the path length estimator method is done as in [11], where the neutral density n_o and temperature T_o are computed from the total time spent by test fluxes in the zones. Ionization and charge exchange rates are then computed from n_o and T_o.

Our pseudo-collision algorithm computes ionization and charge exchange rates directly. For example, the sum over all collisions in a zone, $S(ion) = \Sigma\, \omega_{ion}$, gives the total test flux weight ionized in that zone. Multiplying by the total number of test fluxes N gives the ionization rate in ionizations/sec. Similar sums are made representing charge exchange rates, ionization, and charge exchange energies, exiting currents, power deposition and erosion rates at the walls. The neutral density, n_o, is derived from

$$N \cdot S_{ion}/Vol = n_e\, n_o\, \langle \sigma v \rangle_{e\text{-}ionize},$$

where Vol = zone volume and n_e = local electron density. The average energy $\tilde{E}_i$ of a neutral being ionized is

$$\tilde{E}_i = W(ion)/S(ion),$$

where

$$W(ion) = \Sigma\, \omega_i E,$$

the sum again being over all collisions, with E = energy of the colliding neutral.

One weakness of this scoring method is that scoring events occur only at collisions. To score at each pseudo-collision, we need only to modify the scoring method above by taking for S(ion), for example, the sum

$$S'(ion) = \Sigma\ \rho \cdot \omega_{ion},$$

over all pseudo-collisions, where ω_i is as above, and $\rho = \lambda(min)/\lambda(local)$ = real collision probability. On the average, S'(ion) = S(ion), but the variance in S' is less than that of S, for now a collision requiring n pseudo-collisions deposits n scores instead of 1.

Another weakness is that in regions containing no plasma, our sums are zero since λ(local) is infinite. To compute the neutral density here, we assume a "pseudo-plasma" present, consisting of pseudo-ions ψ whose reaction with an atom, reaction (10) Table I, leaves the atom unchanged in every aspect. We assume the local reaction rate of (10) to be a constant fraction of the total (real) local plasma reaction rates. Neutral density temperatures and pressures can then be computed as above, with the electron quantities replaced by the appropriate pseudo-ion quantities. Even in plasma regions this method of computing neutral temperatures gives the true neutral temperature, since $\langle\sigma v\rangle$ for reaction (10) is a constant fraction of the total local $\langle\sigma v\rangle$.

E. Variance Reduction Techniques

Most collisions occur near the plate, resulting in a wealth of scorings there, compared to very few in regions far away. To improve the variance in these distant regions, we use a standard splitting/Russian roulette algorithm [12]. Using larger zones in regions far from the plate also increases the number of scorings per zone away from the plate, while keeping most resolution

near the plate where it is needed due to the larger gradients in the ionization/charge exchange rates there. Suppression of absorption, described above, increases the number of scorings in the more distant zones by keeping test fluxes alive which otherwise would be killed off by ionization. Finally, our technique of scoring at each pseudo-collision is an improvement over recording the scores only at collisions.

F. Optimization and Performance

Improvements in efficiency at the programming level by factors of 2-3 on a vectorizing machine, such as the CRAY-1, can come from modularizing the particle tracking algorithm shown in Fig. 8 and performing each segment in loops over 64 or 128 test fluxes. The arrays containing test flux data are merged at each step, discarding the test fluxes as they finish their flights. We have found that the added overhead cost of merging is small compared to savings gained from vectorization. The mergers are not easily vectorized, but they consist mostly of assignment statements, while the expensive calculations in particle tracking are now done in vectorized loops.

Performance on the CRAY-1 requires 8-10 CPU sec/1,000 test fluxes for a typical INTOR calculation, with 500-2,000 text fluxes used for a typical profile. The program consists of ~ 4,000 of FORTRAN IV executable statements and uses ~ 40,000 decimal words of array storage.

IV. EXAMPLE CALCULATIONS

A. The Vacuum Case

We modeled the case of molecular flow through a tube of rectangular cross section with width b >> than height a and length ℓ. Clausing [13] has deduced values for $\kappa = Q_f/Q_{in}$, where Q_{in} = incoming current and Q_f = current exiting the far outlet. Table III lists his values of κ along with Q_f/Q_{in} computed by

us for ℓ/a varying from 0.2 to 100, using 10^6 test particles and assuming a cosine distribution in the polar angle to the wall of velocities of reflecting particles.

B. The PDX Scoop Experiment

A "pump-limiter divertor" experiment has been carried out on the PDX experimental device at the Princeton Plasma Physics Laboratory [14]. Figure 2 shows the scoop design, where plasma enters a 2 × 5 × 22 cm chamber mounted near the discharge edge with axis parallel to the field lines, and the density of the neutralized gas is measured at the end of the plenum.

For densities of 1-5 x 10^{12} particles/cm^3 the mean free path lengths are longer than the tube, and the neutrals are not expected to have a strong effect on the plasma. At densities above 10^{13} particle/cm^3, the neutrals interact with the plasma and would be expected to affect the plasma, as the plasma significantly retards the flow of neutrals back to the main plasma. The neutral pressure in the pumping chamber is plotted in Fig. 10. The pressure varies as $n^{0.94}\ T^{0.26}$, while the particle flux at the plate scales as n/T. The slower dependence of the pressure on T ($\sim T^{1/4}$) is due, possibly, to the larger role of electron ionization compared to charge exchange (Fig. 3b) as T_e increases 10 to 50 eV. More of the neutrals are ionized at the higher temperatures and thus are not reflected down into the plenum chamber. The experimental neutral pressure rises more as n^2 than n, indicating that the effect of the neutrals on the plasma must be important.

C. The Proposed INTOR Design

Plasma source rates, the effects of the plasma on helium and hydrogen pumping, the heat loads on the divertor walls and neutralizer plates, and the erosion rates for the neutralizer plate and divertor walls were computed for a variety of INTOR model poloidal divertors and diverted plasmas (Fig. 1).

The first geometry of the divertor chamber considered was similar to that shown in Fig. 1b but with a rectangular instead of hyperbolic throat. Cases were studied with the density having a Gaussian profile of 8.8×10^{12} cm^{-3} at the center falling to 1.1×10^{12} cm^{-3} at the channel walls, and central temperature of 250 eV, varying with the same Gaussian profile as the density. The pumping speed of the pump is approximated by that of a thin slot [13]

$$3.638\ K \cdot ab \cdot \left(\frac{T}{M}\right)^{1/2}\ \text{ℓ/sec}\ , \qquad (3.1)$$

where K is the Clausing factor in Table III, T is in degrees Kelvin, M = 5 the atomic weight of DT, the pump length ℓ = 40 cm, and the width b = 25. Assuming 12 such pumps in the device, a pump width of a = 8 cm provides 24,200 ℓ/sec of pumping for the whole torus.

The relative pumping speeds with the plasma of three such cases varying the throat dimensions are listed in Table IV. The ratio $R = Q_{pump}/Q_{plasma}$, the neutral current of neutral particles returning to the main plasma divided by the neutral current leaving the bottom of the pump, is given for D, T, and He. R_{vac} is the ratio of the geometric (Formula 3.1) pumping speeds of the pump and the return channel to the main plasma.

The ratios of the Monte-Carlo calculations of the various R's to the geometric R_{vac} reflect the effect of the plasma reducing the neutral backflow from the neutralizer plate to the main plasma and in raising the effective pumping speed of the pump. The ratios vary from a value of 20.3 for the 80 × 30 hydrogen case to one of 1.7 for the 50 × 40 helium case.

We note that these three cases scale in a reasonable way. As we make the channel shorter, or wider, relatively more particles return to the main plasma. Applying the formula (3.1) to the 80 × 30 and 50 × 30 cases, the

ratio R should reduce by a factor of 0.81 as the channel length is decreased. The actual reduction is about 0.19 for hydrogen and 0.44 for helium, indicating that the plasma appreciably retards the neutral backflow to the main plasma. Since lengthening the channel increases the ionization and charge exchange "optical depth" of the divertor channel, it is not surprising that the geometric scaling underestimates the effect.

However, since widening the channel for a given length does not increase the optical depth of the channel, one would expect in this case that the geometric scaling in formula 3.1 will be closer to the divertor result. It predicts a reduction in the ratio by a factor of 0.69 from the 50 × 30 case compared to the 50 × 40 case. This is fairly close to the Monte-Carlo results (0.49 for D, 0.56 for T, and 0.52 for He), indicating that one can use the geometric scaling for estimating the effects of varying the channel width.

One interesting feature of these three cases was that in each case relatively more hydrogen than helium was pumped, with R_H/R_{He} ranging from 2.36 to 3.12. This apparent contradiction with the results of Seki et al. [4] led us to compute a fourth case to reproduce their results which were for a rectangular channel 100 cm long and 30 cm wide with a 20 cm wide plasma (47.5% p^+m 47.5% T^+, and 5% He^{++}) with a uniform density and temperature of 250 eV. Their pump model, reflecting a fixed fraction entering the pump opening instead of tracking test fluxes in the pump, and their neutral reflection data were used also by us. However, our more detailed treatment of molecules was retained.

The backflow $B = [\Gamma_{pump}/(\Gamma_{plasma} + \Gamma_{pump})]$ in their calculation varied from 0.7 to 0.46 for DT, and from 0.7 to 0.23 for He as the density varied from 8×10^{12} cm^{-3} to 10^{12} cm^{-3}. Thus their helium enrichment varies from 1 to 2. In particular, their result for a density of 3×10^{12} cm^{-3} has an

enrichment of B_{He}/B_H = 1.13. Our case at that density, yields backflows of 0.66 for D, 0.69 for T, and 0.55 for He. This gives us a helium de-enrichment of B_{He}/B_H = 0.81. However, considering the uncertainties in the wall reflection models, the different atomic physics, and differences in the code, this discrepancy probably is not significant.

Another set of INTOR calculations was carried out for a more realistic hyperbolic geometry (Fig. 1b). Typically, the hydrogen ionization sources are peaked at the neutralizer plate (Fig. 11a) falling gradually toward the divertor throat, and the molecules are ionized at the edge of the plasma (Fig. 11b). Neutral impurities, such as iron, are produced by sputtering at the neutralizer plate and walls. Since the neutral impurity atoms are low energy (~ 3 eV) and heavy (A = 57), their mean free path is short, and they are ionized close to the wall (Fig. 11c).

The energy deposited on the walls and neutralizer plates was computed for a variety of sample plasmas with temperatures varying from 14 eV to 439 eV, and with the density scaled appropriately from 1.85×10^{13} cm^{-3} to 10^{11} cm^{-3} to maintain constant energy flux. The power on the neutralizer plate did not vary greatly (Fig. 12a). They peak at the separatrix at ~ 400 watts cm^{-2} and fall off rapidly. The erosion rates of the divertor plates and walls were calculated also for a 500 eV, 10^{12} cm^{-3} diverted plasma. The erosion rate of the ion plate peaks at 26 cm/year at the separatrix for a 100% duty cycle (Fig. 12b). The erosion rates of the divertor walls are much lower, falling rapidly with distance from the neutralizer plate (Fig. 12c).

ACKNOWLEDGMENTS

The authors thank Drs. Paul Rutherford, John Schmidt, Francis Perkins and Allen Booker for encouragement and useful discussions. They also thank Dr. Owen Robinson for the use of MARLOWE and his assistance in using it.

This work was supported by the U.S. Department of Energy Contract No. DE-AC02-76-CHO-3073.

REFERENCES

[1] International Tokamak Reactor, Zero Phase International Atomic Energy Agency, Vienna (1980).

[2] M. T. ROBINSON et al., Phys. Rev. B 9, 5008 (1974).

[3] J. CALLEN et al., IAEA-CN-38/Y-3, Eighth International Conference on Plasma Physics and Controlled Nuclear Fusion Research, IAEA, Vienna (1981).

[4] Y. SEKI et al., Nuclear Fusion 20, 10 (1980).

[5] M. PETRAVIC et al., "A Cool High Density Regime for Poloidal Divertors," submitted to Phys. Rev. Lett.

[6] R. L. FREEMAN and E. M. JONES, CLM-R 137, Culham Laboratory, Abingdon, Berkshire (1974).

[7] E. M. JONES, CLM-R 175, Culham Laboratory, Abingdon, Berkshire (1977).

[8] J. ROTH, J. BOHDANSKY, W. OTTENBERGER, IPP-9/26, Max-Planck-Institut fur Plasmaphysik (1979).

[9] YU. S. GORDEEV, JETP Letters, 25, 204 (1977).

[10] S. V. PUTVINSKY, private communication.

[11] M. HUGHES and D. POST, J. Comp. Phys. 28, 43 (1978).

[12] J. M. HAMMERSLEY and D. C. HANDSCOMB, Monte-Carlo Methods, Metuchen and Co., London, 1964.

[13] P. CLAUSING, Ann. Physik 12, 404 (1932) p. 961.

[14] R. JACOBSEN, "Preliminary Particle Scoop Limiter Measurements in PDX," unpublished.

TABLE I

(1)	H^o	+ H^+	→ H^+	+ H^o	
(2)	e	+ H^o	→ H^+	+ 2e	
(3)	e	+ H_2^o	→ $2H^o$	+ e	
(4)	e	+ H_2^o	→ H^o	+ H^+	+ 2e
(5)	e	+ H_2^o	→ H_2^+	+ 2e	
(5a)	e	+ H_2^+	→ $2H^o$		
(5b)	e	+ H_2^+	→ H^o	+ H^+	+ e
(6)	He^o	+ He^+	→ He^b	+ He^c	
(7)	He^o	+ He^{++}	→ He^{++}	+ He^o	
(8)	He^o	+ H^+	→ He^+	+ H^o	
(9)	e	+ He^o	→ He^+	+ 2e	
(10)	ϕ	+ atom	→ ϕ	+ atom	

Neutral-Plasma Reactions Included in our Model. H is hydrogen, deuterium, or tritium. We assume that if H_2^o is ionized in reaction (5), then the H_2^+ produced is dissociated instantaneously by reactions (5a) or (5b). Equation 10 is the pseudo-reaction of neutrals with pseudo-ions ϕ used to compute the neutral density and temperature.

TABLE II

$E = F^1(\xi)$(eV)

57.3	100.	127.5	150.8	168.5

$\cos\ \theta = F^2(\eta, \xi)$

0.5104	0.6931	0.8096	0.8926	0.9672
0.4843	0.6817	0.8009	0.8869	0.9654
0.4753	0.6497	0.7727	0.8681	0.9609
0.4646	0.6475	0.7642	0.8642	0.9522
0.3343	0.5088	0.6313	0.7533	0.8867

$\cos\ \psi = \dfrac{F^3(\zeta, \eta, \xi)}{F^3(1, \eta, \xi)}$

-0.9460	-0.5096	-0.0494	0.5299	0.9293
-0.9224	-0.5758	0.0270	0.5498	0.9519
-0.9481	-0.6291	0.0147	0.5343	0.9507
-0.9501	-0.5564	0.0380	0.5548	0.9442
-0.9594	-0.5536	0.1303	0.6682	0.9567

$F^3(2, \eta, \xi)$

-0.9510	-0.6303	-0.1349	0.5591	0.9501
-0.9448	-0.6107	-0.0077	0.4643	0.9378
-0.9362	-0.4654	0.0031	0.5703	0.9513
-0.9322	-0.5519	-0.0030	0.5741	0.9734
-0.9388	-0.5297	0.1150	0.5879	0.9400

$F^3(3, \eta, \xi)$

-0.9308	-0.5249	0.1161	0.6025	0.9511
-0.9346	-0.6454	-0.0176	0.4700	0.9325
-0.9448	-0.5862	-0.0408	0.6021	0.9694
-0.9341	-0.5364	-0.0625	0.5133	0.9494
-0.9474	-0.5254	-0.0254	0.5714	0.9646

$F^3(4, \eta, \xi)$

-0.9095	-0.5492	0.0054	0.5960	0.9142
-0.9395	-0.6243	-0.0676	0.5596	0.9630
-0.9670	-0.5826	-0.0809	0.5839	0.9256
-0.9401	-0.5702	0.0194	0.5559	0.9450
-0.9376	-0.4852	0.0458	0.6537	0.9589

$F^3(5, \eta, \xi)$

-0.9343	-0.6085	-0.0343	0.5889	0.9491
-0.9199	-0.5429	0.0072	0.6042	0.9324
-0.9343	-0.5448	0.0822	0.6140	0.9716
-0.9217	-0.4109	0.1232	0.6503	0.9696
-0.9243	-0.4775	0.0642	0.6172	0.9532

Results from MARLOWE code for incident energy E = 200 eV, polar angle of α = 0°. The fraction of incident particles reflected is 0.4320.

TABLE III

ℓ/a	K_{Cl}	K_{MC}	σ_M
0.1	0.9525	0.9527	0.0002
0.2	0.9096	0.9090	0.0003
0.4	0.8362	0.8360	0.0004
0.8	0.7266	0.7262	0.0004
1.0	0.6848	0.6847	0.0005
1.5	0.6024	0.6023	0.0005
2.0	0.5417	0.5423	0.0005
3.0	0.4570	0.4575	0.0005
4.0	0.3999	0.3984	0.0005
5.0	0.3582	0.3565	0.0005
10.0	0.2457	0.2411	0.0004
50.0	0.0782	0.0799	0.0003
100.0	0.0461	0.0473	0.0002

Ratios Q_f/Q_{in} of the molecular current Q_f leaving the far end of a tube of rectangular cross section a by b and length ℓ, b >> a, b >> ℓ, to the current entering, Q_{in}, as computed by our algorithm (K_{MC}) and by Clausing (K_{Cl}) [1], for ℓ/a = 0.1 to 100. The standard deviation σ_M in the calculation of K_{MC} is $[K_{MC}(1 - K_{MC})/M]^{1/2}$, where M = 10^6 test currents.

TABLE IV

ℓ (cm)	a (cm)	Q_p/Q_t			E	R_{vac}	$C = (Q_p/Q_t)/R_{vac}$	
		D	T	He			DT	He
80	30	2.67	3.83	0.56	3.12	0.16	20.1	1.7
50	30	0.53	0.70	0.25	2.44	0.11	5.0	1.0
50	40	0.26	0.39	0.13	2.36	0.075	4.1	1.7
100	30	1.94	2.20	1.229	1.68			

Relative pumping rates for D, T, and He in rectangular divertors. Divertor throats are ℓ by a cms, and pumps are 8 cm by 40 cm. Q_p and Q_t are the currents leaving the pump and throat respectively. E is the ratio Q_p/Q_t for DT over Q_p/Q_t for He. R_{vac} is the ratio of pump to throat conductances computed for a vacuum using equation (3.1), and C is Q_p/Q_t over R_{vac}.

FIGURE CAPTIONS

Fig. 1a. Poloidal cross section of proposed INTOR Poloidal Divertor configuration.

Fig. 1b. Schematic of the INTOR divertor operation.

Fig. 2. Cross sections of various geometries modeled.

Fig. 3a. $n\langle\sigma v\rangle$ For

1 - $H^{o} + H^{+} \rightarrow H^{+} + H^{o}$, $n = n_{H^{+}} = 1 \times 10^{13}$

2 - $e^{-} + H^{o} \rightarrow H^{+} + 2e^{-}$, $n = n_{e} = 1.1 \times 10^{13}$

3 - $e^{-} + He^{o} \rightarrow He^{+} + 2e^{-}$, $n = n_{e} = 1.1 \times 10^{13}$

4 - $He^{o} + He^{++} \rightarrow He^{++} + He^{o}$, $n = n_{He^{++}} = 0.05 \times 10^{13}$

5 - $He^{o} + H^{+} \rightarrow He^{+} + H^{o}$, $n = n_{H^{+}} = 1 \times 10^{13}$

where H = D/T, $E_{H^{o}} = 3 \times T_{e}$, $E_{He^{o}} = 6 \times T_{e}$, and $T_{i} = T_{e}$.

Fig. 3b. Hydrogen and helium charge exchanging probabilities, $T_{i} = T_{e}$.

Fig. 3c. $n_{e}\langle\sigma v\rangle$ for

1 - $e^{-} + H^{o}_{2} \rightarrow H_{2}^{+} + 2e^{-}$

2 - $e^{-} + H^{o}_{2} \rightarrow 2H^{o} + e^{-}$

3 - $e^{-} + H^{o}_{2} \rightarrow H^{o} + H^{+} + 2e^{-}$

4 - $e^{-} + H^{+}_{2} \rightarrow 2H^{o}$

5 - $e^{-} + H^{+}_{2} \rightarrow H^{o} + H^{+} + e^{-}$

assuming $n_{e} = 1.1 \times 10^{13}$.

Fig. 4. H^{o} and H^{+} yield fractions from H^{o}_{2} dissociation.

Fig. 5. Coordinate system for MARLOWE wall reflection data.

Fig. 6. Sample Test Flux Flight. A triton ion strikes the neutralizer plate, reflects as a T^{o} atom, strikes a wall, desorbs as a TT^{o} molecule, dissociates, undergoes a further sequence of plasma/wall collisions until its weight is less

than a set minimum (here 10^{-6}), where a pure ionization occurs ending the flight.

Fig. 7. Tracking a test flux flight using the path length estimator method: Start at position P_o with velocity V and set $\mu = -\text{Log}(\xi)$, ξ a uniform random number, $0 < \xi < 1$. Compute P_1 and $\mu_1 = d_1/\lambda(\text{local})$ until $\sum \mu_i > \mu$, say at P_n. Then the collision point is at P_c where

$$d_c = \lambda(\text{local}) \left\{\mu - \sum_{i=1}^{n-1} \mu_i\right\}.$$

Fig. 8. Flow chart of the pseudo-collision algorithm.

Fig. 9. Construction of the pseudo-collision algorithm reference arrays.

Fig. 10. Calculation of neutral pressure in plenum of PDX scrape experiment [14].

Fig. 11a. Ionization rate profile for D^+ production in sample 70 × 112.5 cm INTOR divertor.

Fig. 11b. Ionization rate profile for D_2^+ production in sample 70 × 112.5 cm INTOR divertor.

Fig. 11c. Ionization rate profile for Fe^{+1} production in sample 70 cm × 70 cm INTOR divertor.

Fig. 12a. Power loads at the neutralizing plate for the INTOR divertor.

Figs. 12b-c Erosion rates of iron neutralizing plate and divertor walls for a 500 eV, 10^2 cm^{-3} diverted plasma (100% duty cycle).

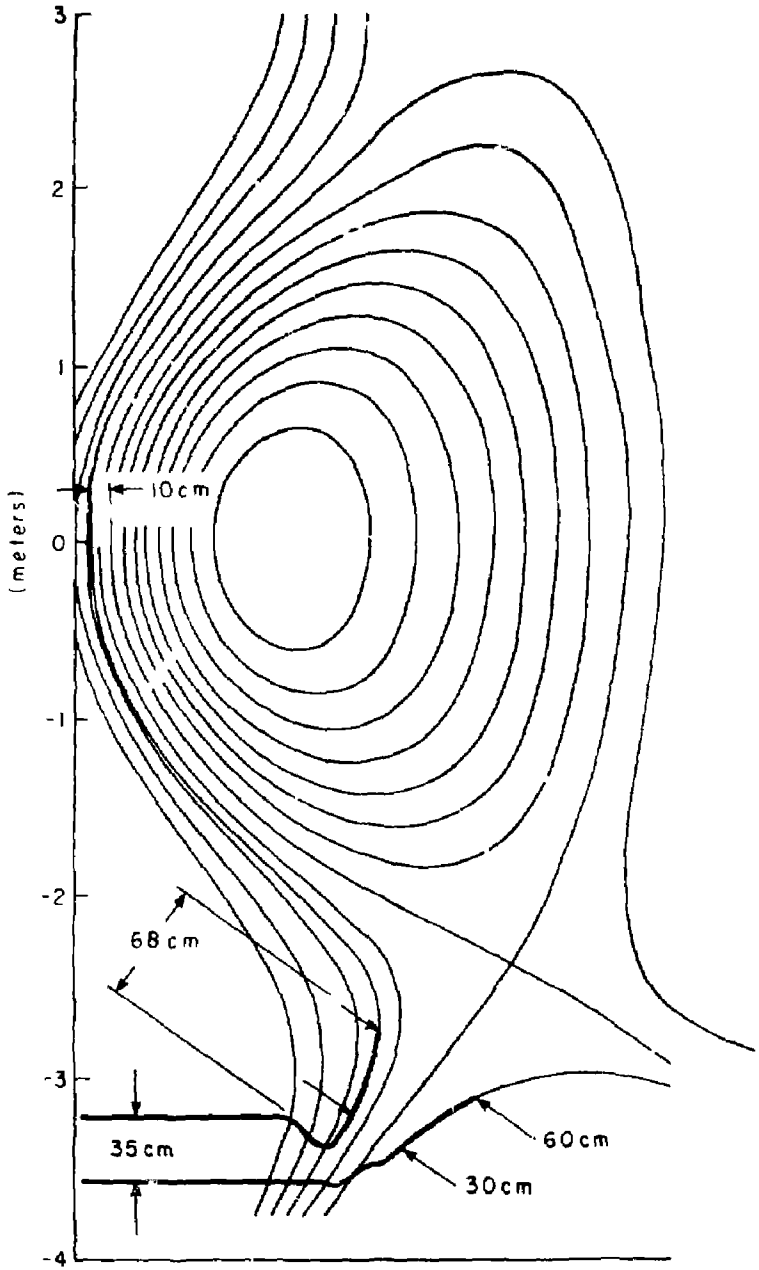

Fig. 1a

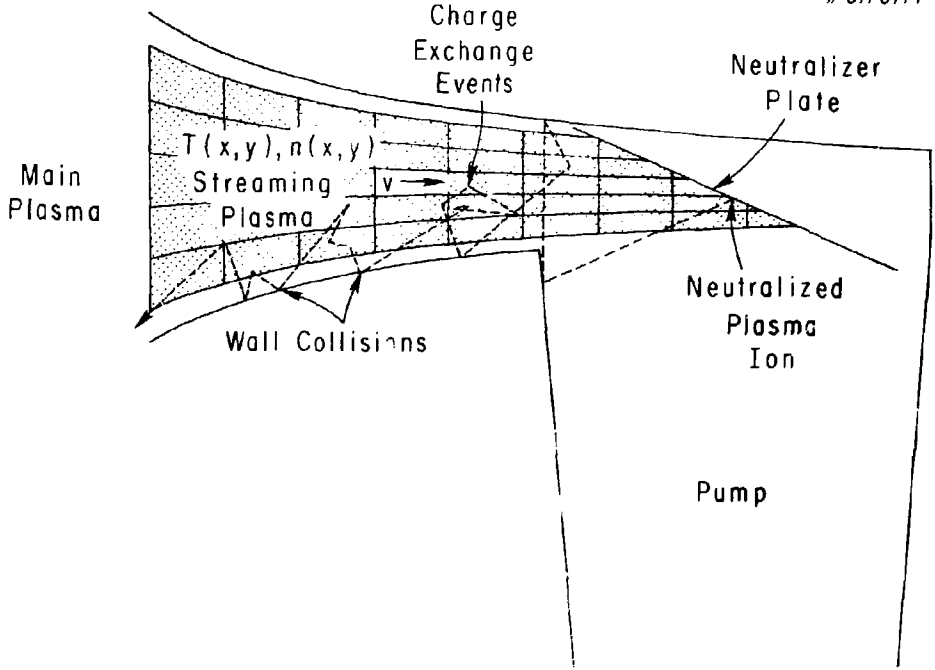
Charge
Exchange
Events
Neutralizer
Plate
T(x,y), n(x,y)
Streaming
Plasma
v
Main
Plasma
Wall Collisions
Neutralized
Plasma
Ion
Pump

Fig. 1:

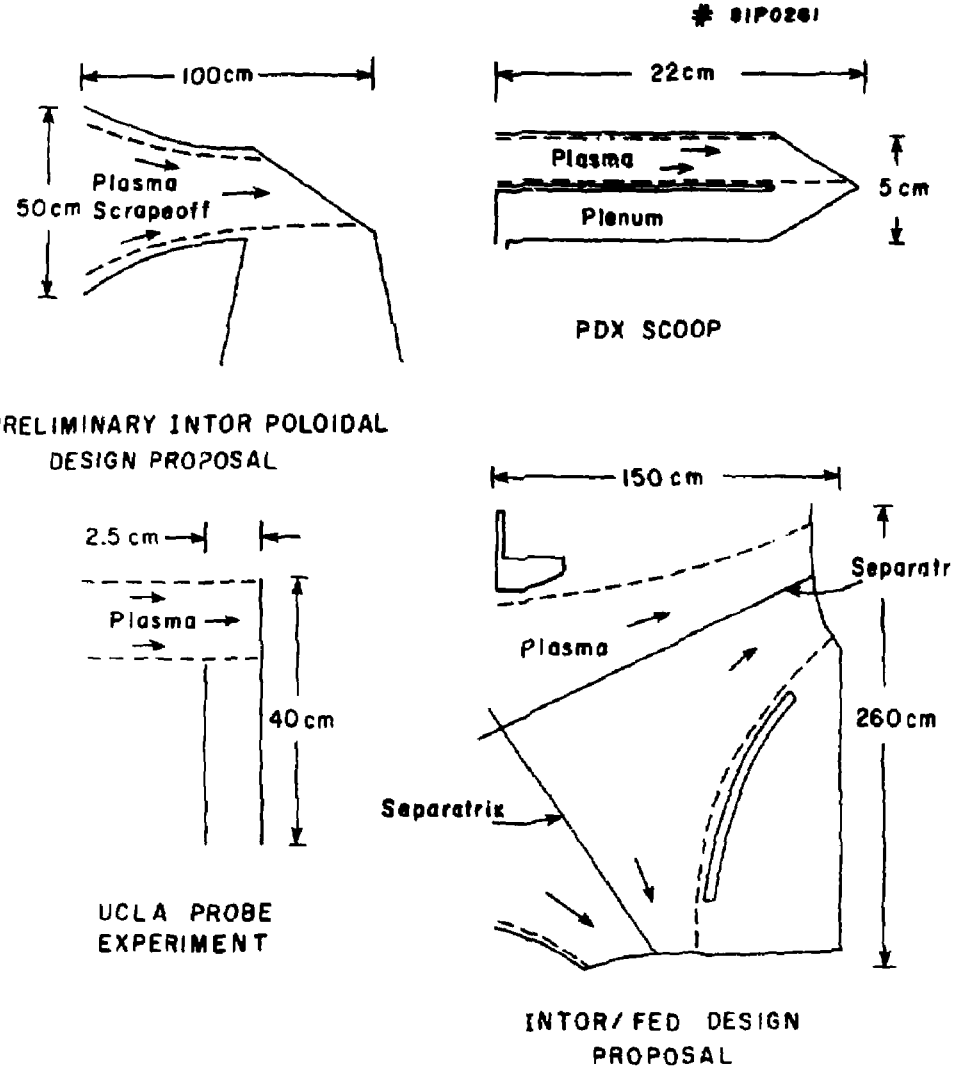
100cm
Plasma
50cm Scrapeoff
PRELIMINARY INTOR POLOIDAL
DESIGN PROPOSAL
22cm
Plasma
Plenum
5cm
PDX SCOOP
2.5 cm
Plasma
40cm
UCLA PROBE
EXPERIMENT
150 cm
Separatrix
Plasma
260cm
Separatrix
INTOR/FED DESIGN
PROPOSAL

Fig. 2

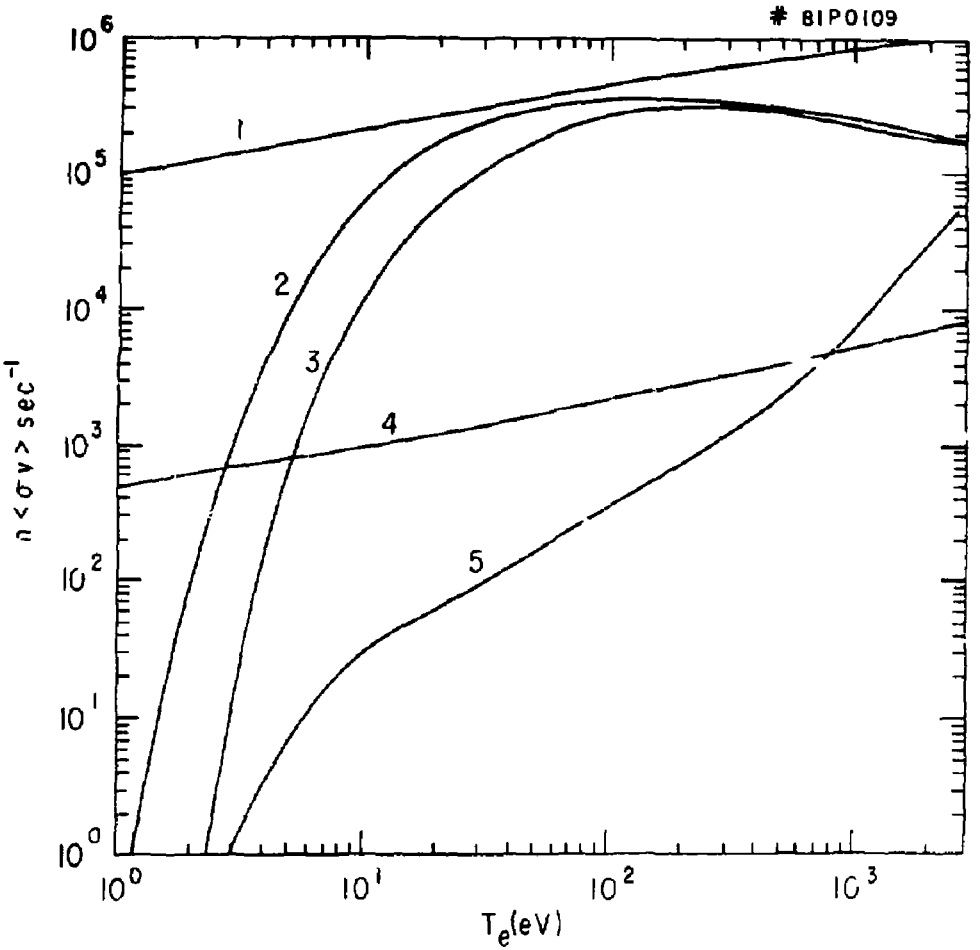
BIP0109
10^6
10^5
10^4
10^3
10^2
10^1
10^0
$n\langle\sigma v\rangle sec^{-1}$
1
2
3
4
5
10^0
10^1
10^2
10^3
$T_e(eV)$

Fig. 3a

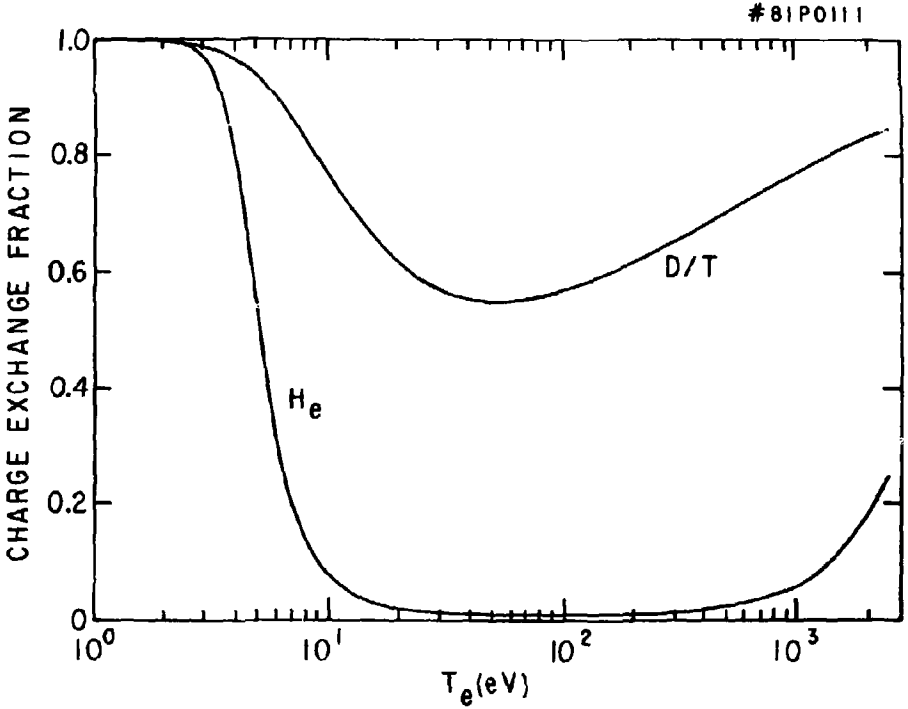
#81P0111
CHARGE EXCHANGE FRACTION
1.0
0.8
0.6
0.4
0.2
0
D/T
He
10^0
10^1
10^2
10^3
T_e(eV)

Fig. 3b

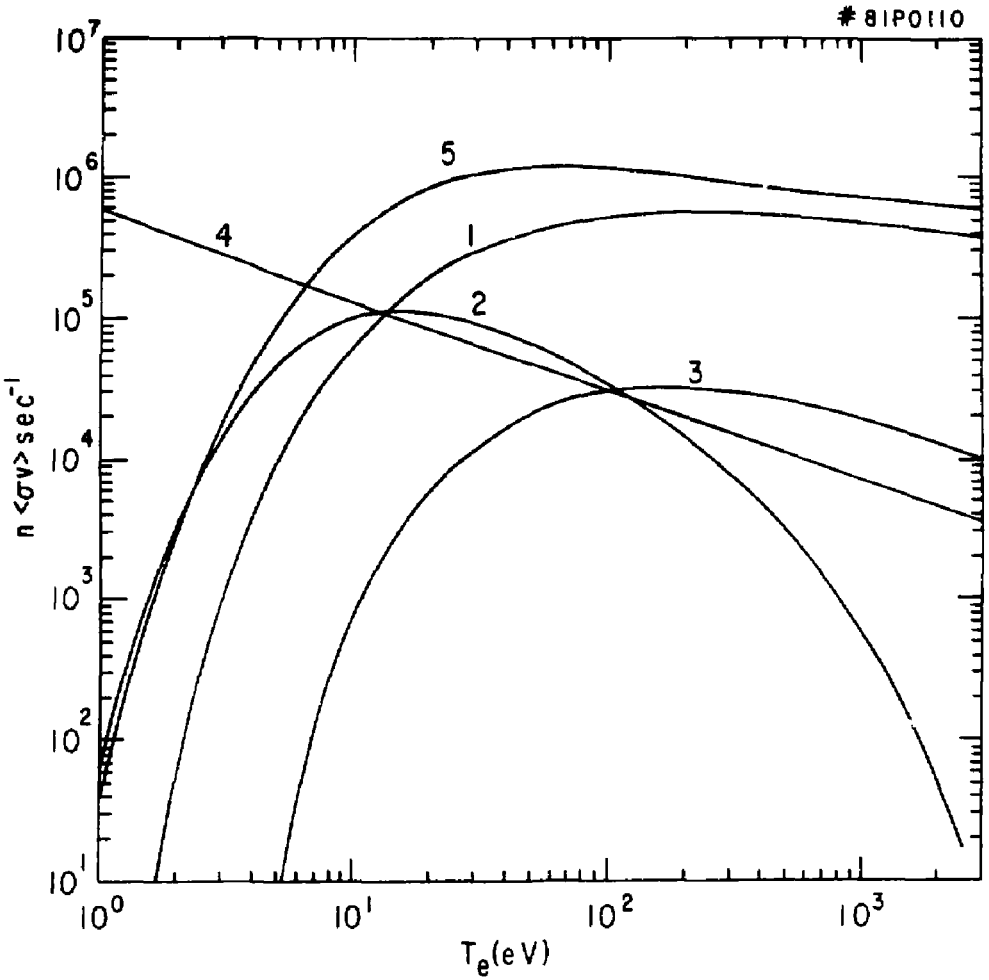
#81P0110
10^7
10^6
10^5
10^4
10^3
10^2
10^1
$n\langle\sigma v\rangle sec^{-1}$
5
4
1
2
3
10^0
10^1
10^2
10^3
$T_e(eV)$

Fig. 3c

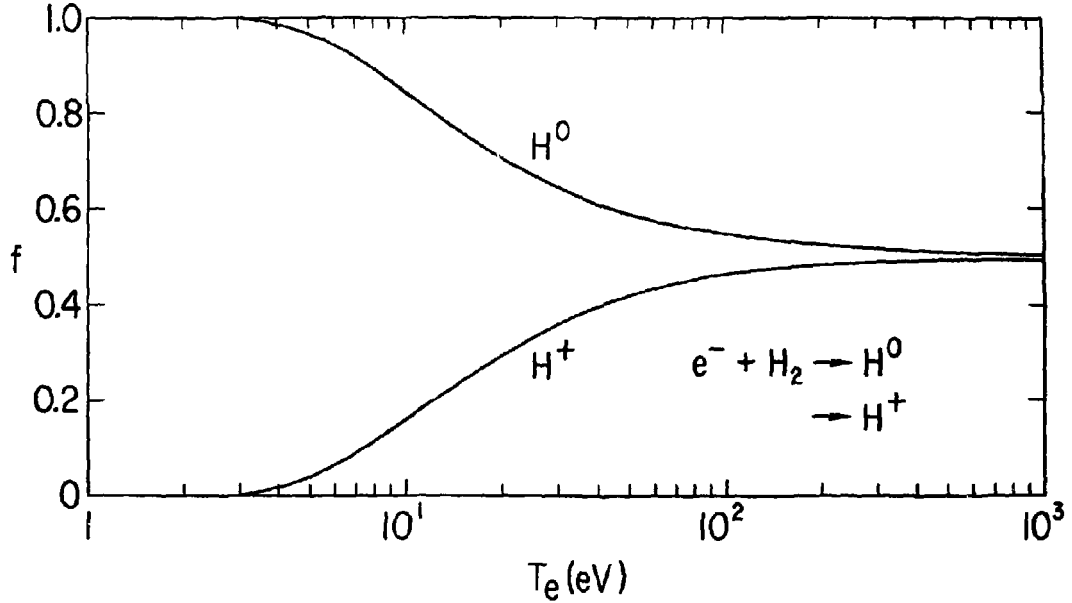

Fig. 4

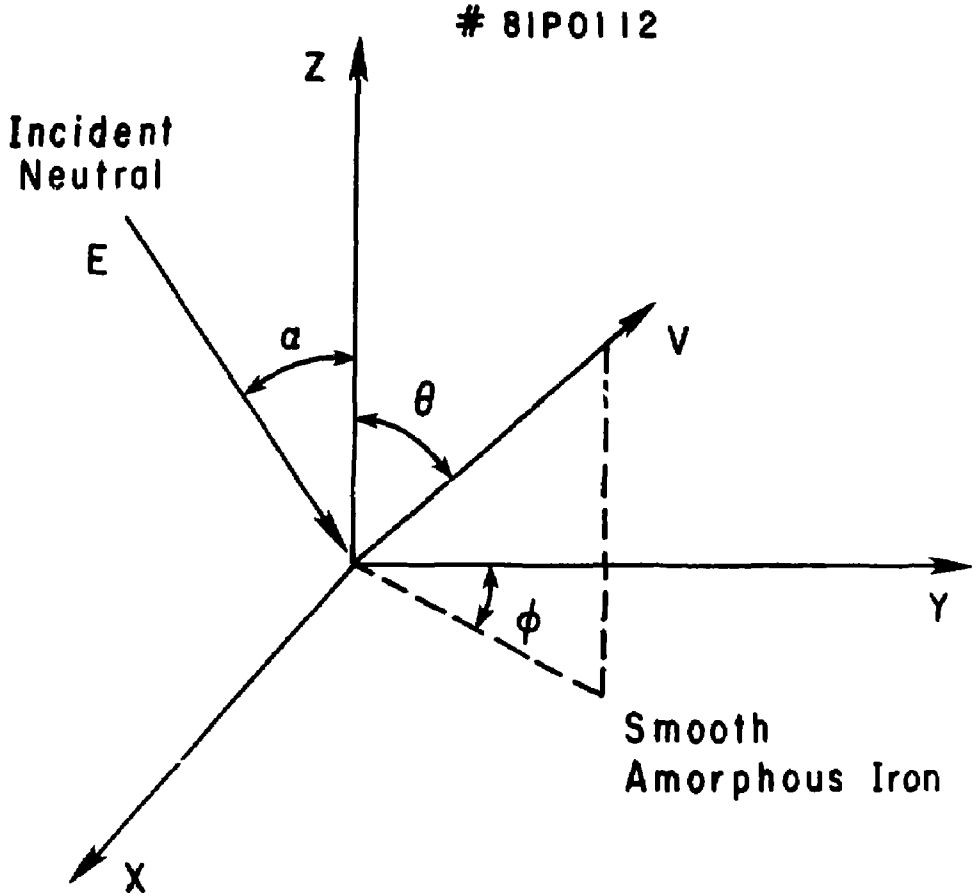

Fig. 5

#81P0178

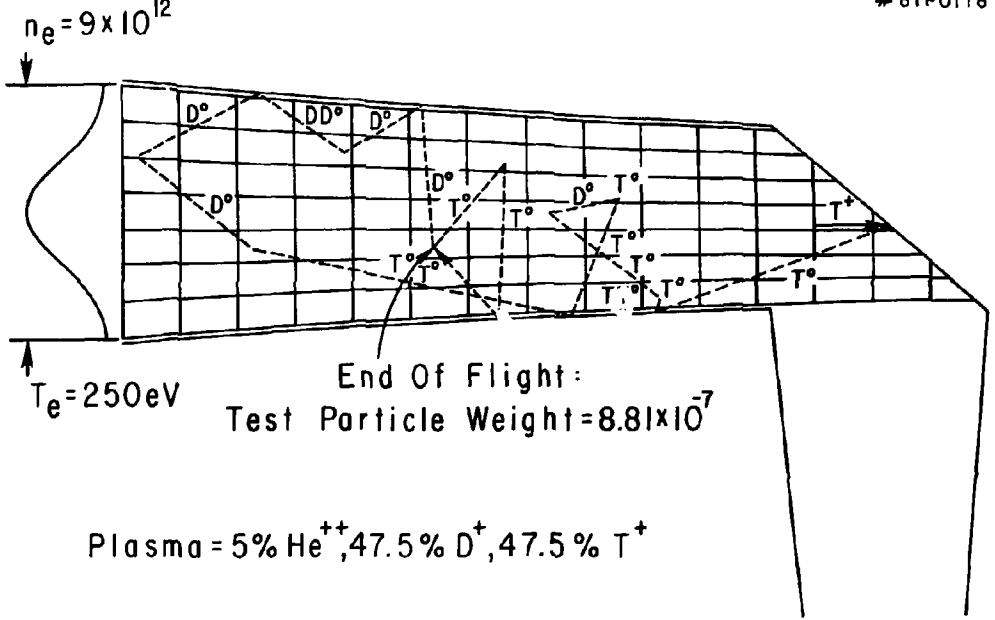

Fig. 6

81P0104

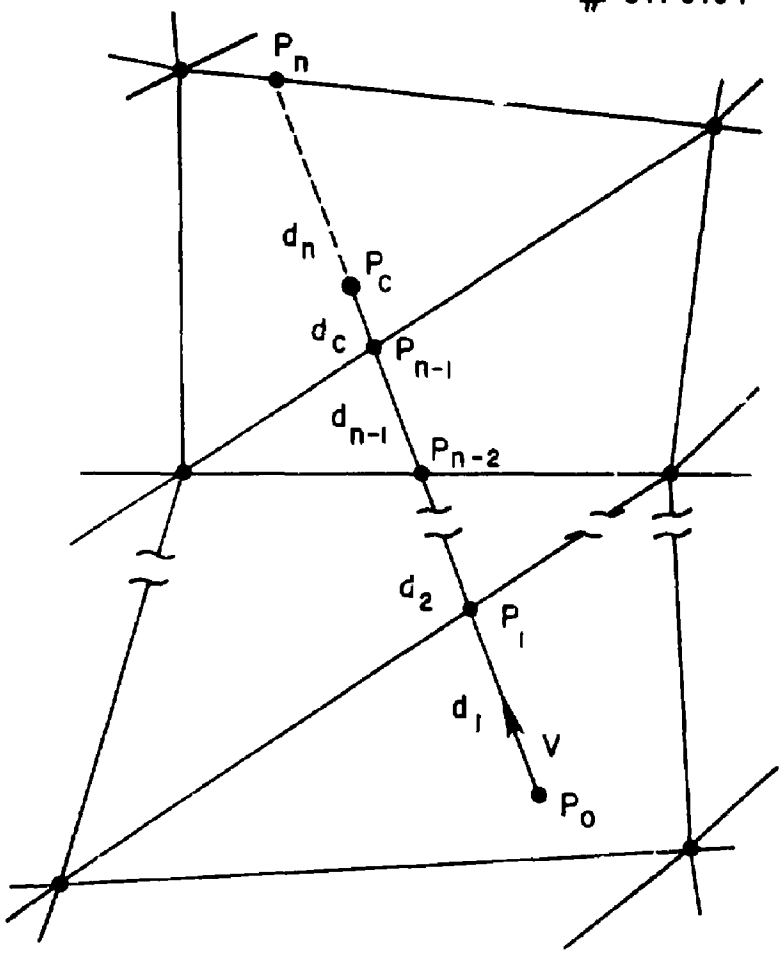

Fig. 7

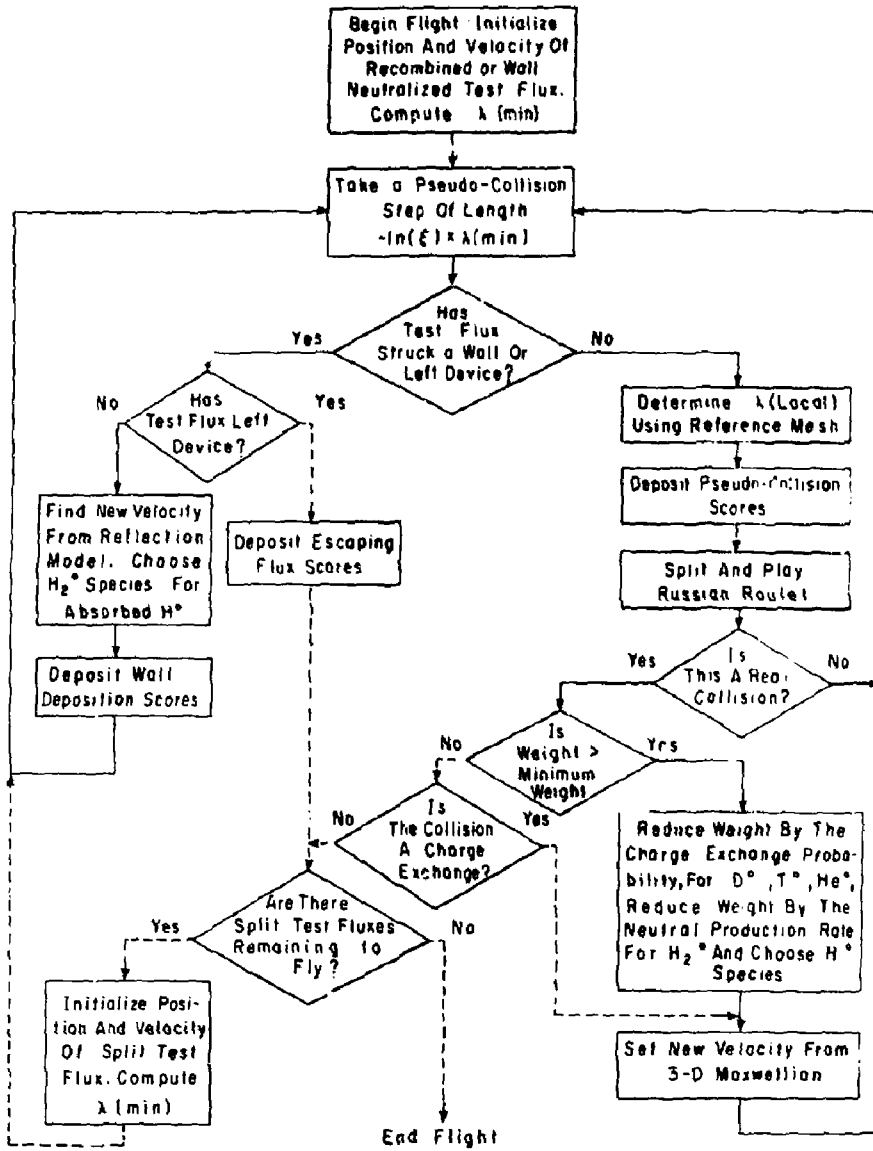

Fig. 8

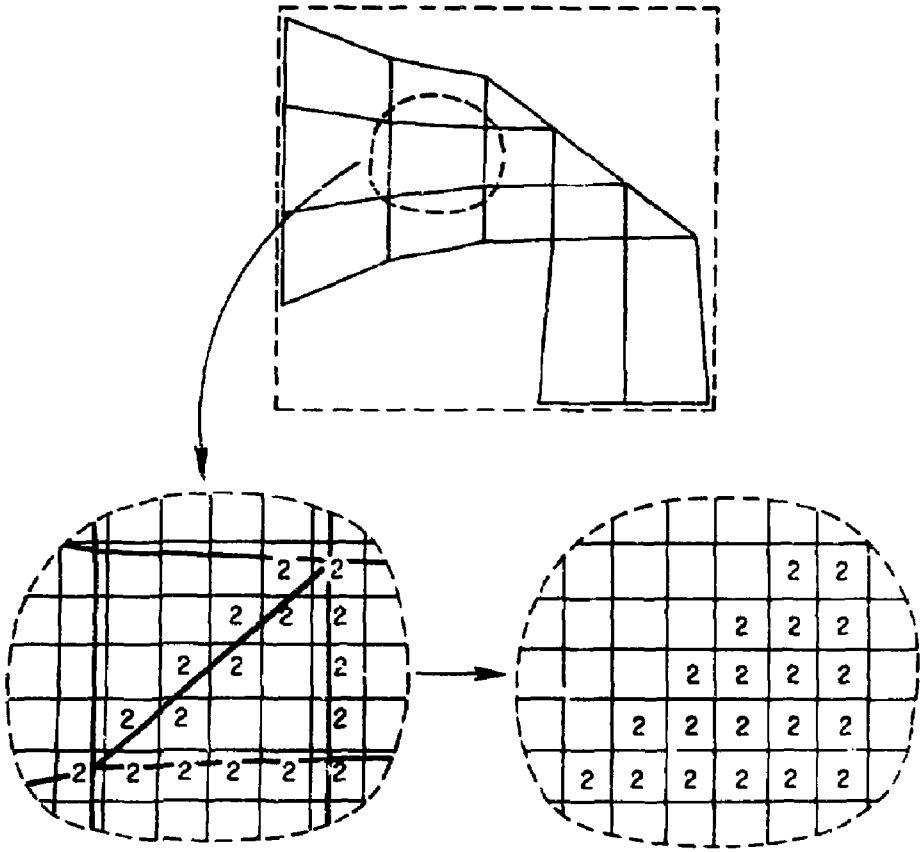

Step 1. Triangle Edges Are Traced Onto Reference Array Using Plasma Zone Zone Index Of The Triangle.

Step 2. Traced Triangle Is Filled In.

Fig. 9

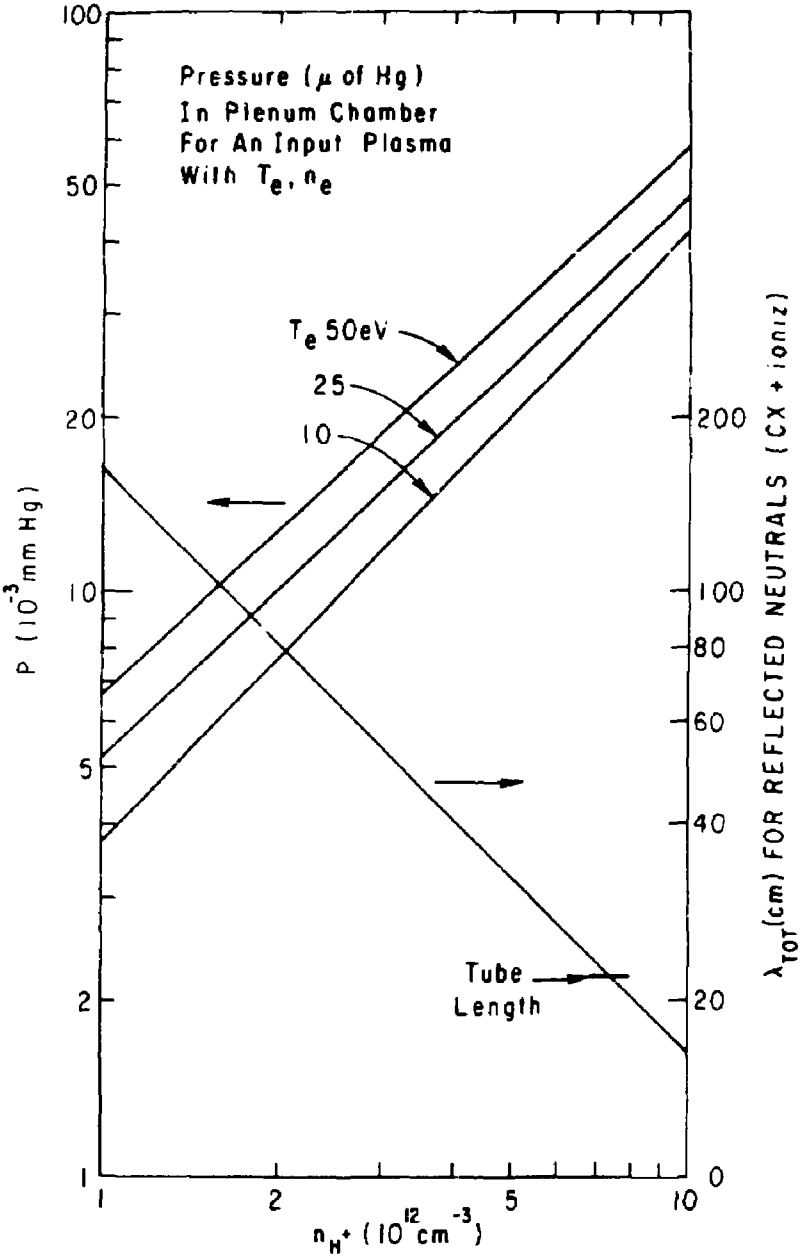
Pressure (μ of Hg)
In Plenum Chamber
For An Input Plasma
With T_e, n_e
T_e 50eV
25
10
Tube
Length
P (10^{-3} mm Hg)
λ_{TOT}(cm) FOR REFLECTED NEUTRALS (CX + ioniz)
n_{H^+} (10^{12} cm^{-3})
100
50
20
10
5
2
1
200
100
80
60
40
20
0
1
2
5
10

Fig. 10

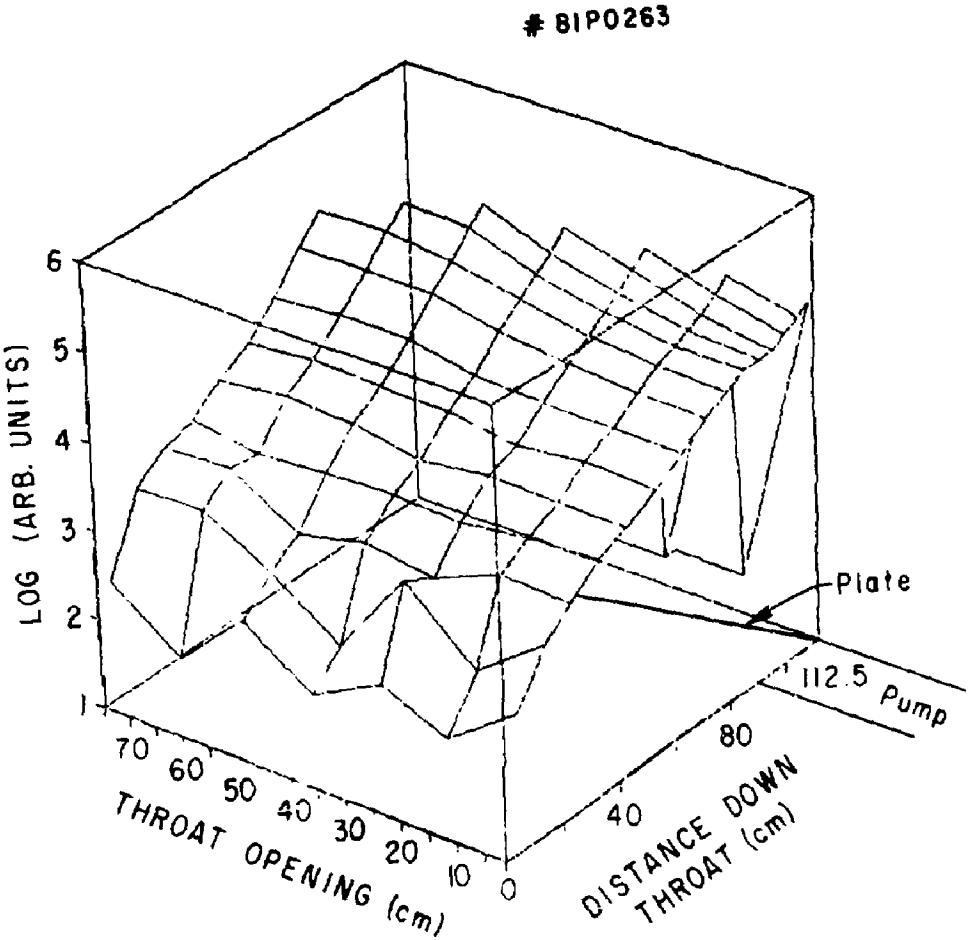
81P0263
LOG (ARB. UNITS)
6
5
4
3
2
1
70
60
50
40
30
20
10
0
THROAT OPENING (cm)
40
80
112.5
DISTANCE DOWN THROAT (cm)
Plate
Pump

Fig. 11a

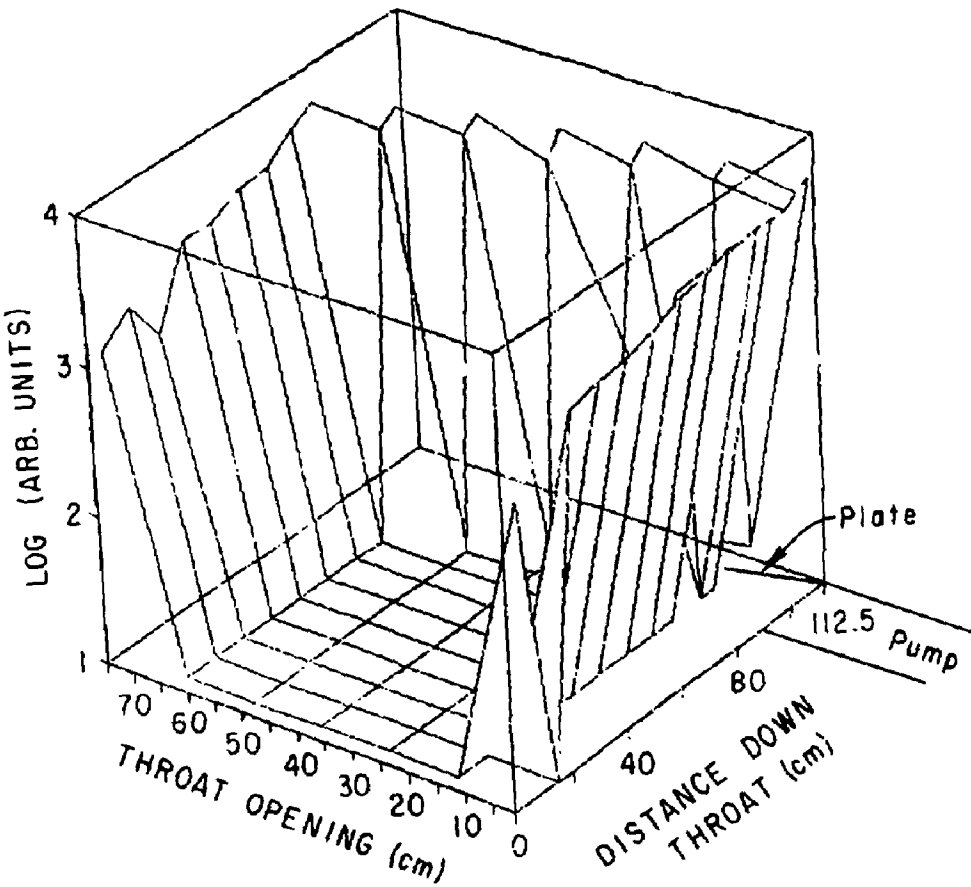
LOG (ARB. UNITS)
4
3
2
1
70
60
50
40
30
20
10
0
THROAT OPENING (cm)
Plate
112.5
Pump
80
40
DISTANCE DOWN THROAT (cm)

Fig. 11b

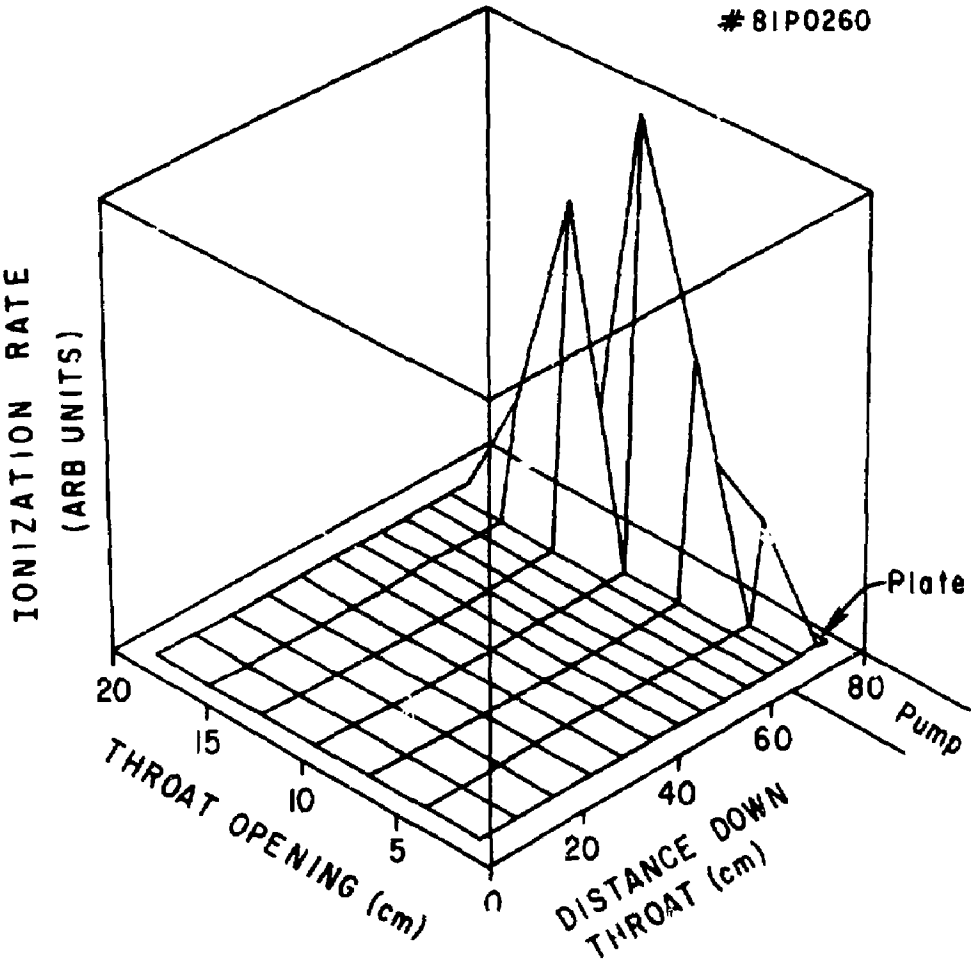
#81P0260
IONIZATION RATE
(ARB UNITS)
Plate
20
15
10
5
0
THROAT OPENING (cm)
20
40
60
80 Pump
DISTANCE DOWN
THROAT (cm)

Fig. 1

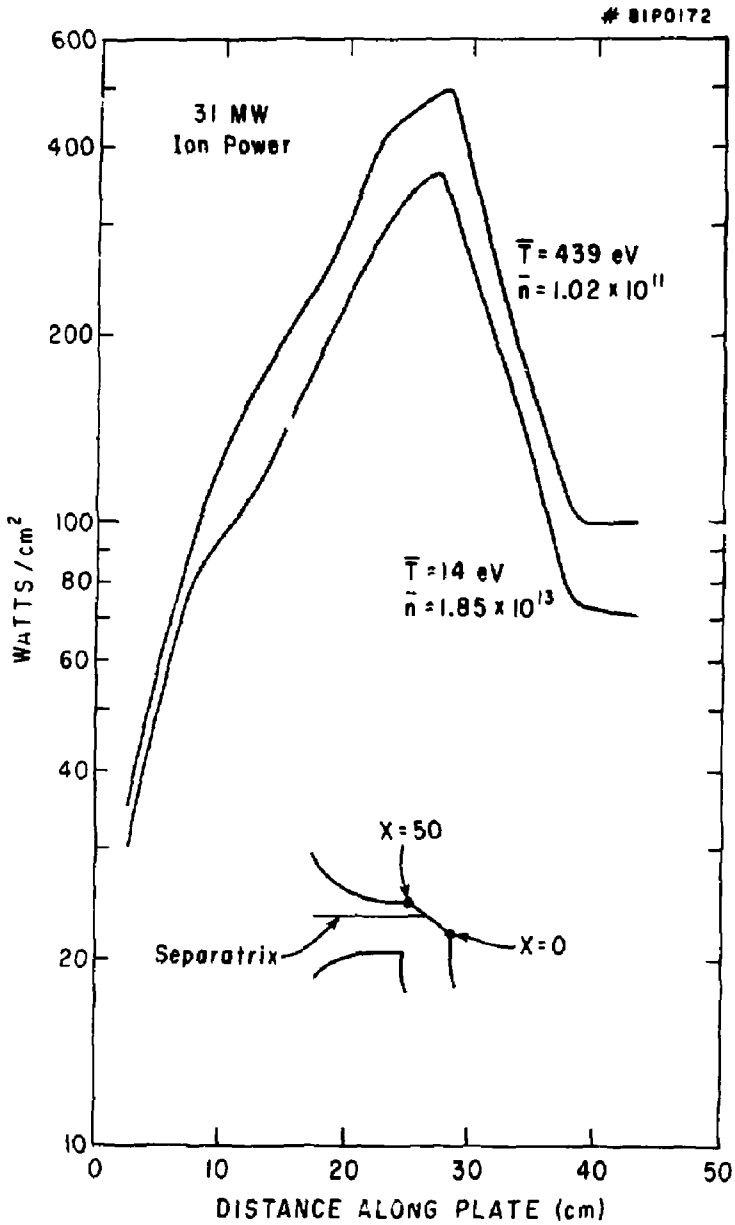
BIP0172
31 MW
Ion Power
$\bar{T}$ = 439 eV
$\bar{n}$ = 1.02 x 10^11
$\bar{T}$ = 14 eV
$\bar{n}$ = 1.85 x 10^13
X = 50
X = 0
Separatrix
WATTS/cm^2
DISTANCE ALONG PLATE (cm)
600
400
200
100
80
60
40
20
10
0
10
20
30
40
50

Fig. 12a

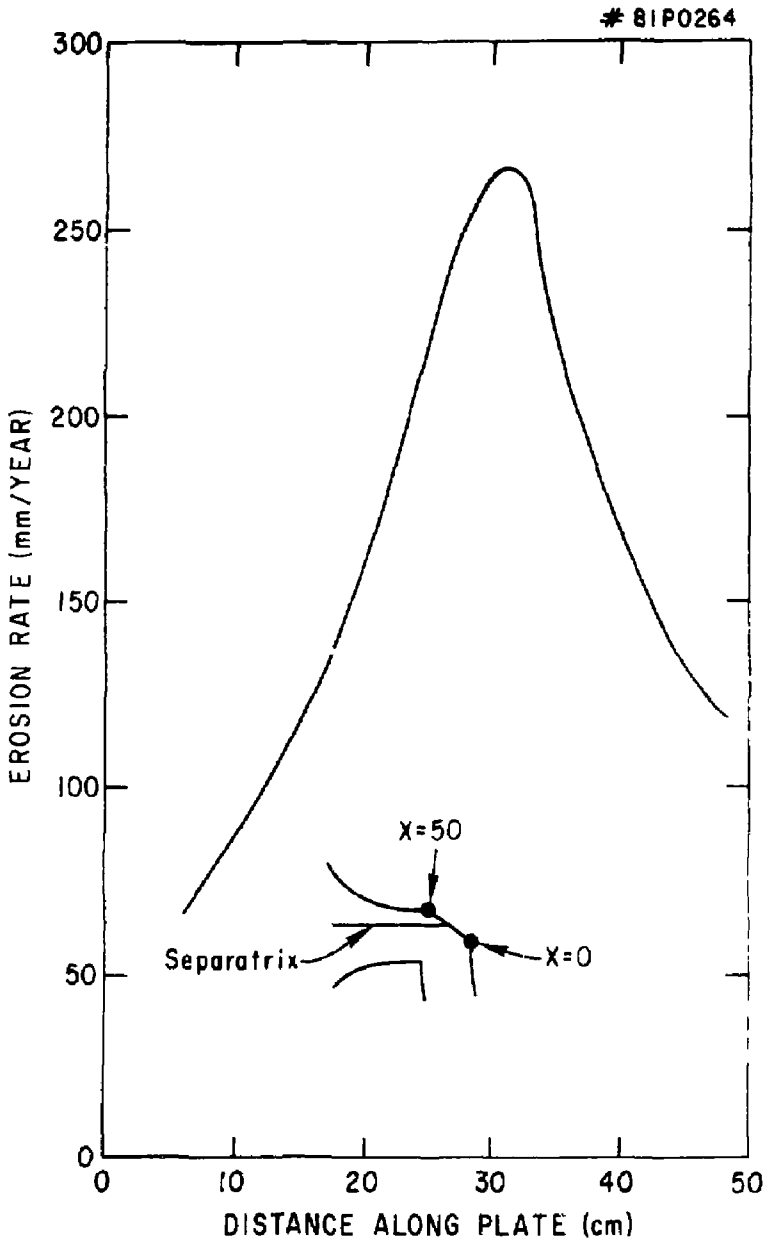
81P0264
300
250
200
150
100
50
0
EROSION RATE (mm/YEAR)
X=50
Separatrix
X=0
0
10
20
30
40
50
DISTANCE ALONG PLATE (cm)

Fig. 12b

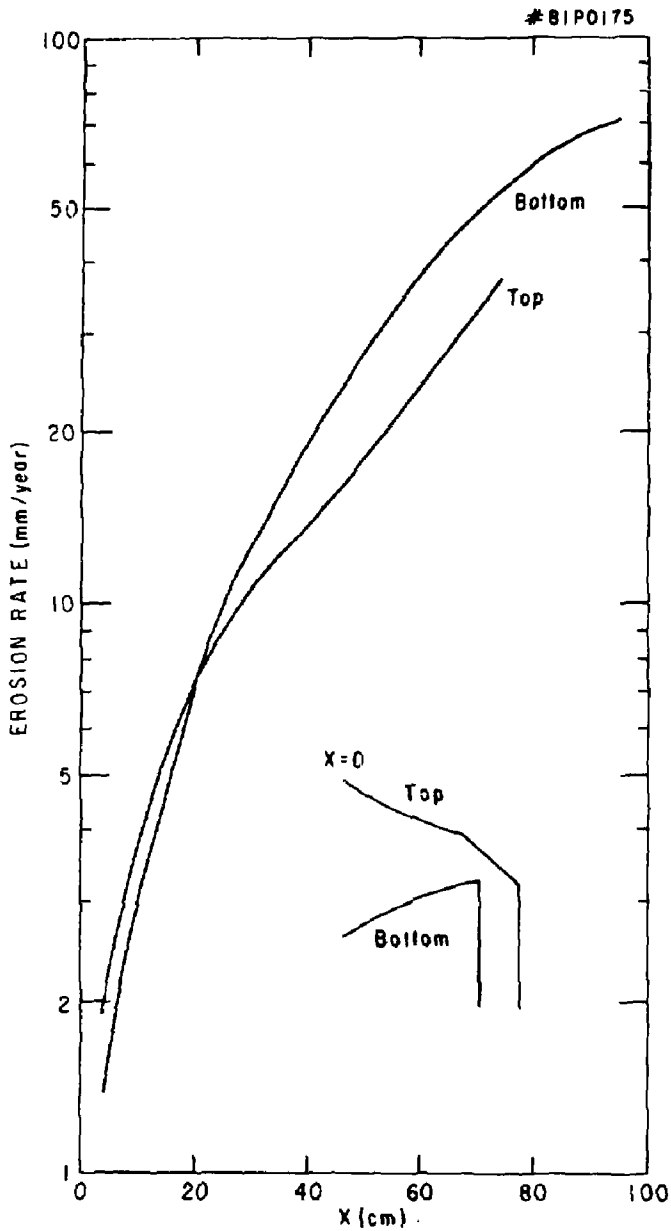
#81P0175
100
50
20
10
5
2
1
0
20
40
60
80
100
X (cm)
EROSION RATE (mm/year)
Bottom
Top
X=0
Top
Bottom

Fig. 12c